PCCP

ROYAL SOCIETY OF CHEMISTRY

PAPER

View Article Online
View Journal | View Issue

Cite this: *Phys. Chem. Chem. Phys.*, 2025, **27**, 16236

Oxygen vacancies assisted photocatalytic dye degradation and photoelectrochemical water splitting performance in Ag and Mg-modified $NaNbO_3$†

Arpita Singha,[a] Mohit Kumar,[b] Phyu Phyu Cho,[b] Sireesha Lavadiya,[c] Sai Santosh Kumar Raavi,[cd] Challapalli Subrahmanyam[b] and Saket Asthana*[a]

A lead-free $Na_{0.85}Ag_{0.15}Nb_{0.95}Mg_{0.05}O_3$ (AM-NN) polycrystalline ceramic was synthesized using the conventional solid-state reaction method, and its structural, dielectric, impedance, and optical properties were thoroughly investigated. X-ray diffraction (XRD) and Rietveld refinement of AM-NN confirmed that the material adopts a perovskite-type orthorhombic structure with the $P2_1ma$ space group. Introducing oxygen vacancies through AgO resulted in spectral changes observed in Raman spectroscopy and Photoluminescence. Dielectric and complex impedance measurements, taken from 10^2–10^6 Hz and room temperature to 500 °C, exhibited non-Debye behavior. AM-NN presented a reduced band gap of 3.12 eV compared to pure $NaNbO_3$ (NN) (3.4 eV) as obtained from UV-vis spectroscopy. AM-NN demonstrated a superior photocatalytic dye degradation percentage of 99% methylene blue (MB), 95% crystal violet (CV) and 60% congo red (CR) at 300 min with the rate constant (k) of 0.0128 min^{-1} (MB), 0.0138 min^{-1} (CV) and 0.0027 min^{-1} (CR), respectively. PEC water splitting showed that the photoanode fabricated with AM-NN exhibits enriched photocurrent density (1.11 mA cm^{-2}). XRD showed no secondary phase after dye degradation, indicating the system's reusability. A detailed investigation into the electrical properties and photocatalytic mechanism was provided to account for the observed improvements in dye degradation and water splitting applications.

Received 28th March 2025,
Accepted 11th July 2025

DOI: 10.1039/d5cp01204j

rsc.li/pccp

1. Introduction

Industrial wastewater containing organic pollutants, such as dyes, surfactants, and fertilizers, has emerged as a significant environmental concern. These pollutants, when released untreated into water bodies, can severely disrupt ecosystems and pose health risks to humans. As a result, a variety of treatment strategies have been explored, including adsorption, filtration, catalytic oxidation, biological methods, and combined processes.[1–4] Among these, photocatalysis has garnered widespread attention due to its potential to efficiently and sustainably degrade complex organic compounds using sunlight or artificial light. Photocatalysis relies on semiconducting materials that absorb light with energy greater than their bandgap, producing electron–hole pairs that can drive redox reactions at the surface. This mechanism is not only useful for environmental remediation but also holds promise in the generation of clean energy, particularly through water splitting to produce hydrogen ions.[5,6] The hydrogen ions produced can contribute to sustainable hydrogen fuel technologies, linking pollution treatment with energy generation.

Over the past decades, more than 50 semiconducting materials—such as TiO_2, ZrO_2, and ZnO—have been studied extensively for their photocatalytic activity. However, challenges like low charge separation efficiency, limited response to visible light, and sluggish kinetics limit their large-scale applications. This has sparked interest in alternative materials and strategies to enhance photocatalytic efficiency. Ferroelectric materials are gaining momentum in this field due to their internal electric fields that help to separate photogenerated charge carriers and suppress recombination.[7,8]

Ferroelectrics possess spontaneous polarization and lack of inversion symmetry, both of which contribute to improved

[a] *Department of Physics, Advanced Functional Materials Laboratory, Indian Institute of Technology Hyderabad, Kandi, Sangareddy 502284, Telangana, India. E-mail: asthanas@phy.iith.ac.in*
[b] *Department of Chemistry, Indian Institute of Technology Hyderabad, Kandi, Sangareddy 502284, Telangana, India*
[c] *Department of Physics, Ultrafast Photophysics and Photonics Laboratory, Indian Institute of Technology Hyderabad, Kandi, Sangareddy 502284, Telangana, India*
[d] *Department of Climate Change, Indian Institute of Technology Hyderabad, Kandi, Sangareddy 502284, Telangana, India*

† Electronic supplementary information (ESI) available. See DOI: https://doi.org/10.1039/d5cp01204j

photocatalytic behaviour. Their internal electric fields can work similarly to the built-in potential of a p–n junction in conventional semiconductors, aiding in better charge separation and carrier mobility.[9–12] A particularly promising ferroelectric material is sodium niobate ($NaNbO_3$). With its stable perovskite structure, earth-abundant composition, environmental friendliness, and strong ferroelectric properties, $NaNbO_3$ is well-suited for photocatalytic applications.[13–15] To further improve performance, researchers have explored loading $NaNbO_3$ with noble metals such as Ag, Au, Pt, and Pd, which can increase surface reactivity and enhance light absorption.[16,17] In this study, Ag^+ and Mg^{2+} were specifically selected as substituents to enhance the photocatalytic performance of $NaNbO_3$, particularly for dye degradation and water splitting applications. Ag^+ is known to improve charge separation efficiency by acting as an electron sink and enhancing visible light absorption, which boosts catalytic activity.[18,19] Meanwhile, Mg^{2+} plays a crucial role in maintaining an optimal concentration of oxygen vacancies and improving charge carrier mobility, both essential for efficient photocatalysis.[20,21]

However, while noble metal modification and doping have shown promise, methods involving precious metals often suffer from high material costs and complex synthesis. A more cost-effective and scalable approach involves defect engineering, particularly through the controlled introduction of oxygen vacancies. These vacancies act as electron traps, improving carrier separation and enabling visible-light-driven activity. For example, Di *et al.*[22] demonstrated that surface oxygen vacancies in $BiFeO_3$ facilitate the rapid separation of photogenerated charges and enhance photocatalytic performance. However, an excess of oxygen vacancies can introduce bulk defects that act as recombination sites, ultimately reducing efficiency. Similar observations have been reported in NBT-based systems, where moderate concentrations of oxygen vacancies improved charge carrier mobility and surface reactivity.[23–26] Therefore, maintaining an optimal balance of vacancies is essential. To achieve this balance, Mg^{2+} ion doping has been proposed as an effective route. Magnesium can help regulate oxygen vacancy concentration by providing pathways for ion migration, which improves both ionic conductivity and charge transport.[21] This strategy offers a practical route to tailor material properties and enhance the overall photocatalytic efficiency of $NaNbO_3$-based systems.

Therefore, investigating the photocatalytic properties of NN-based systems has become a crucial issue in the fields of environmental protection and energy conservation. The current study on AM-NN significantly diverges from existing literature by focusing on the rapid degradation of pollutants such as methylene blue (MB), crystal violet (CV), congo red (CR), and rhodamine B (RhB) through the use of oxygen vacancies. In this work, AgO was used instead of Ag_2O, as it facilitates the formation of a higher concentration of oxygen vacancies, further enhancing photocatalytic activity. A mechanism for dye decolorization driven by the enhanced oxygen vacancies has been proposed. Additionally, the improved photocatalytic water splitting performance, with a photocurrent density (1.11 mA cm^{-2} at 1.2 V *vs.* Pt) is highlighted. Thus, this work offers an approach for eliminating harmful dye molecules from wastewater and promoting water splitting using abundant solar energy, contributing to environmental sustainability.

2. Experimental details

Sodium niobate ($NaNbO_3$), abbreviated as NN, has been synthesized *via* a conventional solid-state sintering route. High-purity analytical grade Na_2CO_3 and Nb_2O_5 (99.99%, Sigma Aldrich, USA) have been used as starting precursors. The powders have been accurately weighed according to the stoichiometric ratio and thoroughly mixed using an agate mortar and pestle for 3 hours with isopropyl alcohol (IPA) as the mixing medium. The homogenized mixture has been calcined in an oxygen atmosphere at 950 °C for 5 hours. After calcination, 1 wt% polyvinyl alcohol (PVA) has been added to the powder as a binder. The granulated powder has been pressed into circular pellets of 10 mm diameter using a uniaxial press. The green pellets have been sintered in air at 1150 °C for 3 hours. For electrical measurements, silver electrodes have been applied to the polished pellet surfaces and heated at 200 °C for 2 hours to ensure good electrical contact.

The Ag^{2+} and Mg^{2+} substituted composition, $Na_{0.85}Ag_{0.15}Nb_{0.95}Mg_{0.05}O_3$, abbreviated as AM-NN, has also been synthesized using the same solid-state sintering technique. The starting precursors, Na_2CO_3, AgO, Nb_2O_5, and MgO (99.99%, Sigma Aldrich Chemicals, USA) powders, have been weighed precisely according to the desired stoichiometry. The powders have been mixed using a mortar and pestle for 3 hours with IPA as the solvent. The resulting mixture has been calcined in an oxygen environment at 950 °C for 5 hours. After calcination, 1 wt% PVA has been added as a binder, and the granulated powder has been pressed into 10 mm diameter discs. The pellets have been sintered in air at 1150 °C for 3 hours. For electrical characterization, silver electrodes have been fabricated and heated at 200 °C for 2 hours.

To characterize the materials, X-ray diffraction (XRD) patterns have been collected at room temperature using a Rigaku SmartLab diffractometer. The surface morphology has been examined using scanning electron microscopy (SEM, Zeiss Supra 40). ImageJ software has been used to estimate the average grain size. The temperature- and frequency-dependent dielectric properties have been measured using a Novocontrol Alpha-A dielectric analyzer. The photoluminescence (PL) spectra of the modified system have been recorded at room temperature using a spectrofluorometer (FLS 1000, Edinburgh Instruments). The ultraviolet-visible (UV-vis) diffuse reflectance spectra have been analyzed using a PerkinElmer Lambda 1050 UV/vis/NIR spectrophotometer.

The photocatalytic performance of the synthesized NN and AM-NN samples has been evaluated by monitoring the degradation of dyes such as rhodamine B (RhB, ≥97.0%, Avra), methylene blue (MB, ≥98%, Sigma-Aldrich), crystal violet (CV, ≥86%, Sigma-Aldrich), and congo red (CR, ≥35%, Sigma-Aldrich) under visible light irradiation using a 500 W halogen

lamp. For each test, 50 ml of a 10 mg l^{-1} dye solution has been mixed with 50 mg of the photocatalyst (NN or AM-NN). The mixture has been stirred in the dark for 30 minutes to reach adsorption–desorption equilibrium. During photocatalysis, at 60-minute intervals over 5 hours, 4 ml of the suspension has been extracted, centrifuged at 8000 rpm for 10 minutes, and the absorbance of the supernatant has been measured using the spectrophotometer in the 200–800 nm range.

3. Results and discussion

3.1. Invariance of structural phase in AM-NN

The powder X-ray diffraction (XRD) patterns of pure NN and AM-NN are shown in Fig. 1. Only diffraction lines of the orthorhombic phase were observed at room temperature for both systems. The diffraction data were utilized for further structural refinement and phase analysis with the help of the Full Proof program.[27] Table 1 presents the lattice parameters and other structural details obtained from the Rietveld refinement. The compounds have an orthorhombic crystal structure with a $P2_1ma$ space group. Substituting Ag and Mg in NN does not induce any changes in the Bragg peak positions.

The tolerance factor (t-factor) for pure NN and AM-NN is calculated to be 0.975 and 0.971 respectively, suggesting that the variation between the two systems is relatively small. As a result, no differences are seen in the XRD analysis. Although the t-factor value of approximately 0.97 is favorable for a cubic structure, the lattice distortion present in some ceramics may result in an orthorhombic phase, which explains the orthorhombic phase we observed.[28] The average crystalline size and lattice strain are estimated using the Debye–Scherrer formula. Incorporating Ag and Mg into NN leads to a decrease in crystallite size from 75 nm to 62 nm and an increase in lattice strain from 0.16 to 0.22 (a detailed calculation of crystalline size and lattice strain is mentioned in the ESI†).

Table 1 Rietveld refinement parameter of NN, and AM-NN

Parameter	NN orthorhombic	AM-NN orthorhombic
Lattice parameter (Å)	a = 5.5721(4) b = 7.7726(8) c = 5.5129(3) $\alpha = \beta = \gamma = 90^\circ$	a = 5.5717(1) b = 7.7695(2) c = 5.5132(5) $\alpha = \beta = \gamma = 90^\circ$
R_p	21.1(2)	21.3(1)
R_{wp}	17.2(1)	17.6(3)
χ^2	2.32(4)	2.34(2)

3.2. Evidence of increased oxygen vacancy in AM-NN using Raman spectroscopy

Fig. 2(a) and (b) present the Raman spectra of NN and AM-NN, offering valuable insights into the vibrational modes associated with the NbO_6 octahedron. The Raman spectra of both materials are deconvoluted into individual peaks to analyze the phonon vibrations. A total of 12 peaks are observed in both systems, representing six distinct vibrational modes: $v_1(A_{1g})$, $v_2(E_g)$, $v_3(F_{1u})$, $v_4(F_{1u})$, $v_5(F_{2g})$, and $v_6(F_{2u})$ as shown in Fig. 2(c). Among these, A_{1g}, E_g, and F_{2g} are Raman-active modes, while F_{1u} and F_{2u} are infrared-active and inactive, respectively.[29–32] In the 180–276 cm^{-1} range, the triply degenerate $v_5(F_{2g})$ and $v_6(F_{2u})$ modes reflect the internal dynamics of the NbO_6 octahedron in both systems. The band around 429 cm^{-1} corresponds to the antisymmetric bending of the $v_4(F_{1u})$ mode, with sharper peaks observed in the modified system compared to the pure NN, indicating a significant bending of the $v_4(F_{1u})$ mode. The most prominent bands at 560 cm^{-1} and 600 cm^{-1} correspond to the $v_2(E_g)$ and $v_1(A_{1g})$ modes, respectively, which are critical for understanding the material's structural integrity. There is no splitting observed around 600 cm^{-1}, suggesting a well-ordered NbO_6 octahedron, which is important for short-range structural order. The band at 670 cm^{-1} is attributed to the $v_3(F_{1u})$ mode, and this band is more significant in AM-NN as shown in Fig. 2(d), similar to the v_1, v_2, and v_4 modes, indicating the NbO_6 octahedron's influence and presence of

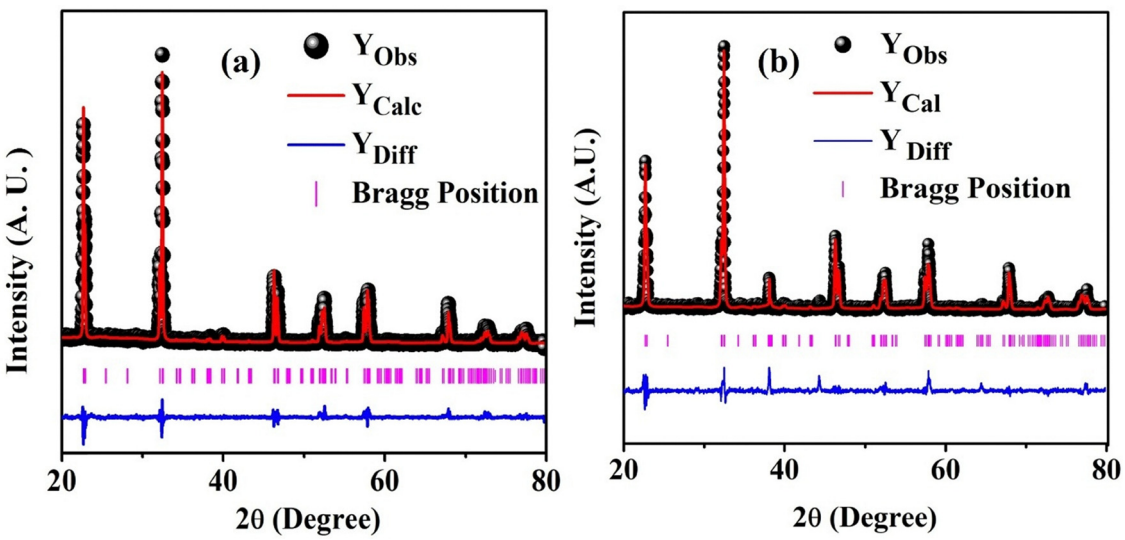

Fig. 1 Shows the XRD patterns of (a) NN and (b) AM-NN.

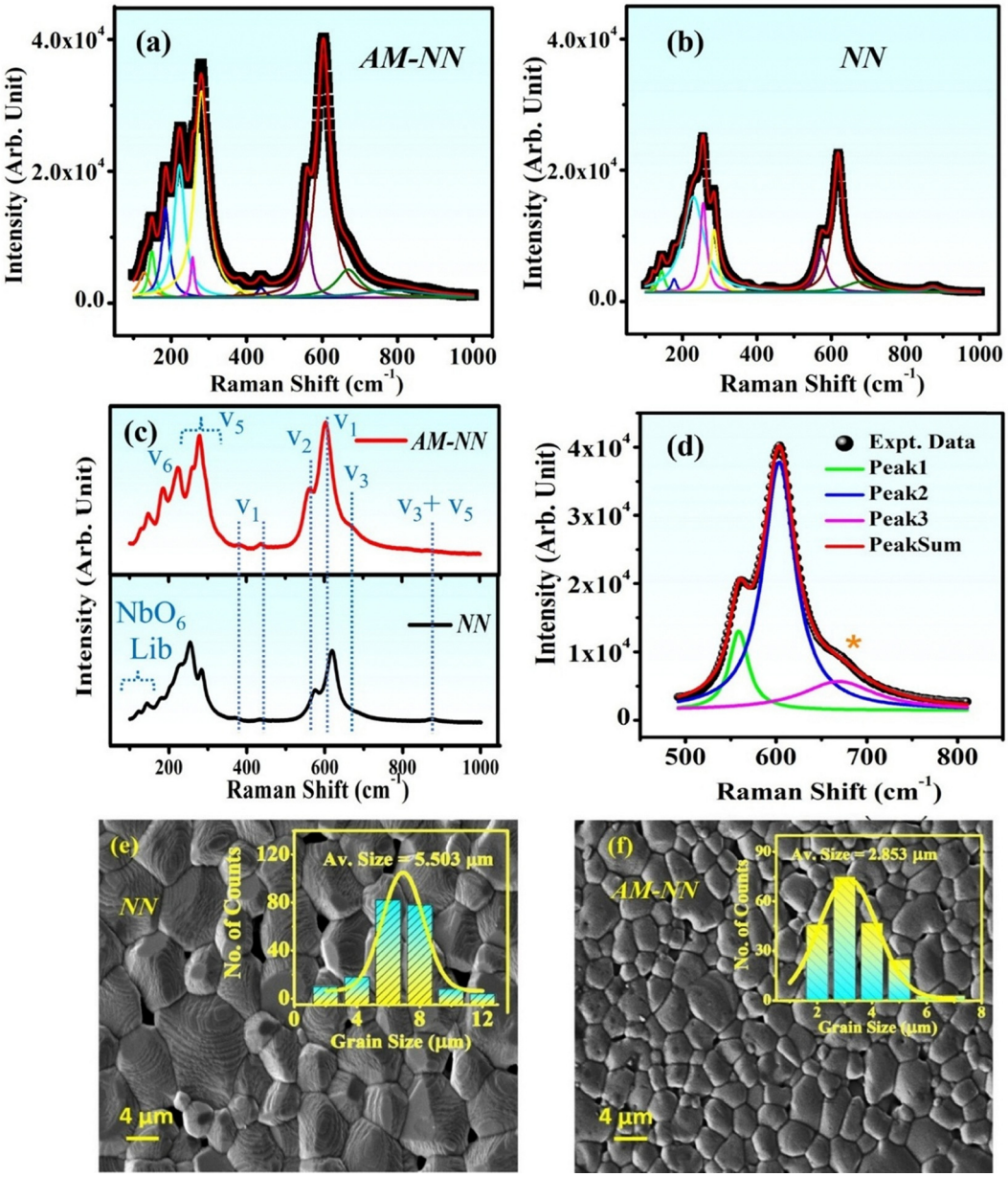

Fig. 2 Raman scattering spectra of (a) NN and (b) AM-NN with Lorentzian fitting (c) comparative Raman spectra indicating different modes (d) deconvolution of v_1, v_2, and v_3 mode of AM-NN system and SEM images of (e) the pristine NN (f) AM-NN systems.

oxygen vacancy.[33–35] Additionally, the weak band at 870 cm^{-1} is linked to the combination of v_1 and v_5 modes, revealing the complexity of vibrational changes within the material. The comparative Raman spectra in Fig. 2(c) reveal both enhanced peak intensities and sharper peaks in the AM-NN system. A comparative table of the peak position of this work and some other related work is listed in Table 2 suggesting a noticeable red shifting of the bands as compared to NN. This combination of increased peak sharpness and downshifted peaks highlights the significant changes in the material's vibrational properties due to the modifications. Previous studies by Chapron *et al.*[37] and Silva *et al.*[38] have discussed the role of oxygen vacancies in causing peak downshifting and intensity enhancement due to localized charge perturbation around vacancy sites. The introduction of oxygen vacancies in the AM-NN system accounts for the observed spectral changes, further supporting their presence and impact on the material's vibrational properties. Following the structural analysis, a microstructural examination is carried out to explore the material's surface morphology and grain distribution.

3.3. Microstructural evidence of defects linked to oxygen vacancies in AM-NN

Scanning electron microscopy (SEM) is crucial in advancing our understanding of material properties at a small scale, facilitating the design and optimization of new materials. Fig. 2(e) and (f) shows the SEM of NN and AM-NN compounds. Pure NN displays larger grains with 5.503 µm and higher density.

Table 2 The Raman band positions observed in the Raman spectra of AM-NN are compared with literature values

	Ref. 36	Ref. 33	Ref. 29	This work	This work
Raman vibrational modes	NN (cm^{-1})	NN (cm^{-1})	NN (cm^{-1})	NN (cm^{-1})	AM-NN (cm^{-1})
v_1	599.4–613.3	605	600	618	604
v_2	556.4–569.4	560	560	573	562
v_3	670	—	—	—	668
v_4	375, 433	377.3, 433.1	429	375, 430	371, 427
v_5	223, 258, 279	~200–300	206–276	~255–285	~250–290
v_6	170	180–186	180	~120–180	~125–185
$v_1 + v_5$	870.6	—	—	874	860

The substitution of Ag and Mg on grain size is observed in grain size reduction (*i.e.* 2.374 μm) and a few distinct pores. Possible explanations for the decrease include the substitution of ions with different radii. Choi *et al.*[39] and Kobayashi *et al.*[40] have suggested that smaller grain sizes often increase oxygen vacancies, driven by the larger surface area and higher energy states at grain boundaries. Phase-field simulations have validated this observation, which reveal a strong link between smaller grain sizes and enhanced elastic and piezoelectric properties in ferroelectric materials such as $BaTiO_3$. The reduction in grain size observed in AM-NN, as compared to NN, can likely be attributed to this effect. Furthermore, the influence of grain size reduction on the electrical properties has been confirmed in earlier studies on NN-based systems.

3.4. Confirmation of elemental states and oxygen vacancies *via* XPS

Fig. 3(a)–(e) displays the high-resolution XPS spectra of AM-NN system corresponding to Na 1s, Nb 3d, O 1s, Ag 3d, and Mg 1s, respectively. Similarly, the high-resolution XPS spectra of NN are shown in Fig. S1(a)–(c) (ESI†), corresponding to Na 1s, Nb 3d, and O 1s, respectively. The presence of all the constituent elements in both AM-NN and NN systems is confirmed from the high-resolution XPS spectra.

In Fig. 3(a), the Na 1s orbital is identified by a peak centred at 1071.6 eV.[41] The high-resolution Nb 3d spectrum, shown in Fig. 3(b), displays two distinct peaks corresponding to the spin–orbit components. The peak at 207.1 eV is attributed to Nb $3d_{5/2}$, while the peak at 210.0 eV corresponds to Nb $3d_{3/2}$.[42] As shown in Fig. 3(c), the O 1s high-resolution spectrum reveals three separate components with binding energies at 529.5, 531.2, and 533.8 eV. Similarly, the high-resolution O 1s spectrum of NN presented in Fig. S1(c) (ESI†) is deconvoluted into three distinct peaks located at 529.4, 531.0, and 534.3 eV. The comparative O 1s spectra for AM-NN and NN, presented in Fig. 3(f), show broader peaks in the AM-NN sample, indicating an enhanced concentration of oxygen vacancies in the modified AM-NN system. The increased oxygen vacancy concentration can facilitate improved charge carrier separation, which is beneficial for photocatalytic activity. Moreover, these vacancies can act as active sites for surface reactions, further enhancing the overall photocatalytic efficiency.[43,44] As shown in Fig. 3(d), the high-resolution Ag 3d spectrum displays a characteristic doublet, with peaks located at 366.6 eV and 375.0 eV, corresponding to the Ag $3d_{5/2}$ and Ag $3d_{3/2}$ components, respectively. This doublet may be due to the coexistence of Ag(I) and Ag(II) or Ag(II) oxidation states, which is consistent with the use of AgO as the precursor. Typically, a single peak at 368.6 eV would be observed for pure Ag(I); however, the presence of an additional peak confirms the mixed-valence state.[45] As illustrated in Fig. 3(e), the high-resolution spectrum of Mg exhibits a prominent peak at 1304.0 eV, corresponding to the Mg 1s orbital and confirming its successful incorporation.[46]

3.5. Temperature and frequency-dependent dielectric behaviour of AM-NN and NN

Fig. 4(a) and (b) presents the comparative dielectric curves of AM-NN and NN under (a) varying temperature and (b) frequency conditions. It is observed that the dielectric constant of the AM-NN system is notably lower than that of the parent NN system. One possible explanation for this reduction is the presence of oxygen vacancies, as previously discussed in ref. 47. Oxygen vacancies contribute to the enhancement of electrical conductivity by acting as charge carriers, which increases electron mobility; however, this also leads to a decrease in the dielectric constant due to the increased movement of electrons. Fig. 4(c) and (d) illustrate how the dielectric constant and dielectric loss of the AM-NN system (shown in the inset) vary with frequency at different temperatures (RT, 50, 100, 200, 300, 400, and 500 °C). Fig. 4(e) and (f) show that as the frequency increases, the dielectric constant decreases, initially dropping from lower values and eventually levelling off. Electronic polarization plays a more significant role at higher frequencies, while at lower frequencies, mechanisms like space charge and dipolar polarization are more dominant. Therefore, the dielectric constant at higher frequencies is smaller than at lower ones. Additionally, as the frequency increases, the dipole no longer follows the oscillating electric field, reducing the dielectric constant. At room temperature, the dielectric loss remains relatively low across various frequencies. However, at elevated temperatures, the dielectric loss shows a sharp increase, which can be attributed to two main factors: (a) temperature-induced scattering of charge carriers and (b) the presence of defects or impurity phases formed during the sample's preparation,[48,49] for the modified system defects like oxygen vacancies play an important role for this sharp increase. Further, the pure NN is reportedly transitioning at 360 °C from orthorhombic to tetragonal phases.[50] However, upon doping Ag and Mg with NN, a diffused transition temperature (T_C) is observed around 410 °C. There is an appearance hump in the temperature-dependent tangent loss curves at high temperatures (around 400 °C) may be attributed to the presence of relaxation

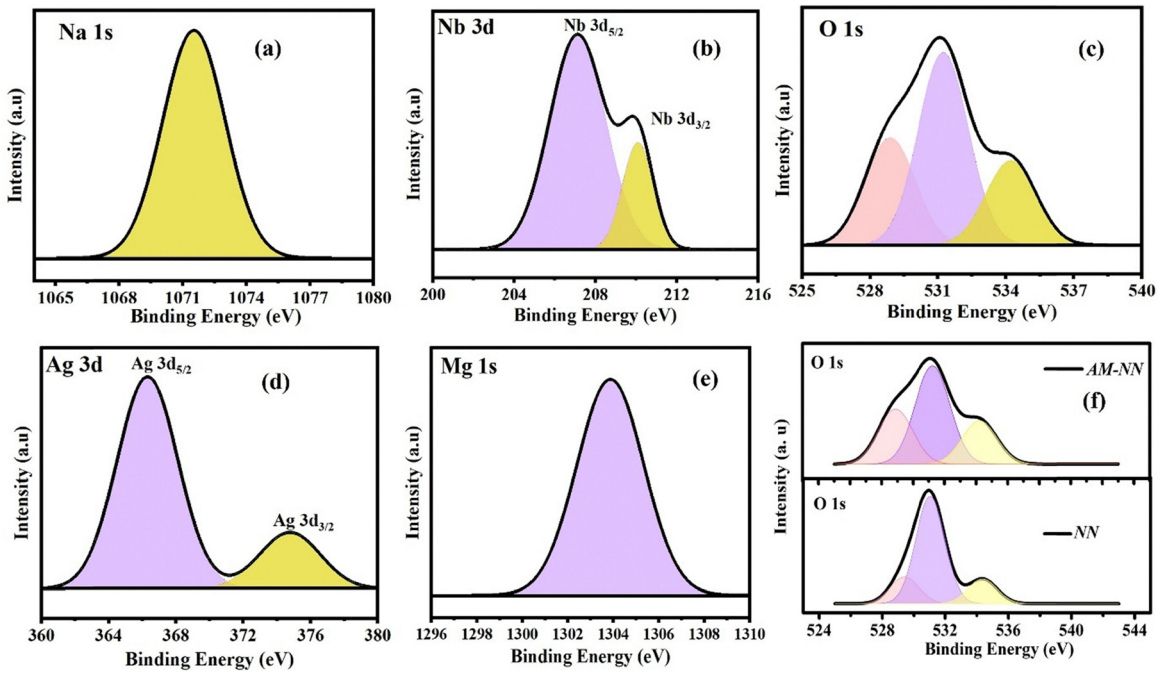

Fig. 3 High-resolution XPS spectra of (a) Na 1s, (b) Nb 3d, (c) O 1s, (d) Ag 3d, (e) Mg 1s, and (f) comparative O 1s spectra for AM-NN and NN.

processes within the material. Compositional disorders or impurities can lead to the occurrence of multiple relaxation phenomena in the solid solution, contributing to the observed humps in the tangent loss.[50] The existence of either a single relaxation time or a distributed relaxation time can be obtained using theoretical models such as the Debye equation and the non-Debye equation.

The Debye equation describes dynamic polarization in materials with a single relaxation time, assuming that the material undergoes a simple exponential decay in polarization when subjected to an external electric field. The Debye equation is given by:[51]

$$\varepsilon_r^* - \varepsilon_{r\infty} = \frac{\varepsilon_{rs} - \varepsilon_{r\infty}}{1 + i\omega\tau}$$

The frequency-dependent dielectric values of NN and AM-NN are fitted with the Debye equation (as shown in the ESI† of Fig. S2). As observed, the Debye equation fits the experimental data of NN well, but it does not provide a good fit for the experimental data of AM-NN.

On the other hand, the Havriliak–Negami equation offers a more accurate fit for most experimental results, particularly for systems that exhibit more than one relaxation process. The Havriliak–Negami equation is expressed as:[48]

$$\varepsilon_r^* - \varepsilon_{r\infty} = \frac{\varepsilon_{rs} - \varepsilon_{r\infty}}{[1 + (i\omega\tau)^{1-\alpha}]^{\beta}}$$

In this equation, the parameters α and β lie within the ranges $0 < \alpha < 1$ and $0 < \beta < 1$.

The frequency-dependent dielectric curves of AM-NN align well with the Havriliak–Negami equation, while the dielectric curves of NN do not, suggesting that the AM-NN system exhibits more than one relaxation process, as shown in Fig. 5. The parameters α and β represent the dispersion of the system (from the fitting, it is obtained that all the α and β values range from 0.41 to 0.86 and 0.5 to 0.89, respectively) and indicate deviations from classical ferroelectric behavior.[52] The parent NN and AM-NN system impedance study is performed for further analysis.

3.6. Investigating the electrical characteristics of AM-NN systems *via* impedance spectroscopy

Complex impedance spectroscopy is a technique commonly used to study the electrical properties of polycrystalline materials across a broad frequency range and at various temperatures. Understanding the contributions from grains, grain boundaries, and interfaces is crucial, as these factors significantly affect the overall electrical behaviour of the material. It is well-established that the complex impedance parameters can be described by specific mathematical relations, which account for the influence of these different structural components.

$$\varepsilon^* = \varepsilon' - i\varepsilon''$$

$$Z^* = Z' - iZ''$$

$$M^* = M' - iM''$$

$$Y^* = Y' - iY''$$

$$\sigma^* = \sigma' - i\sigma''$$

$$\tan\delta = \frac{\varepsilon''}{\varepsilon'} = \frac{Z'}{Z''} = \frac{Y'}{Y''}$$

In this context, ε^* represents the complex dielectric constant, M^* denotes the complex modulus, Z^* is the complex

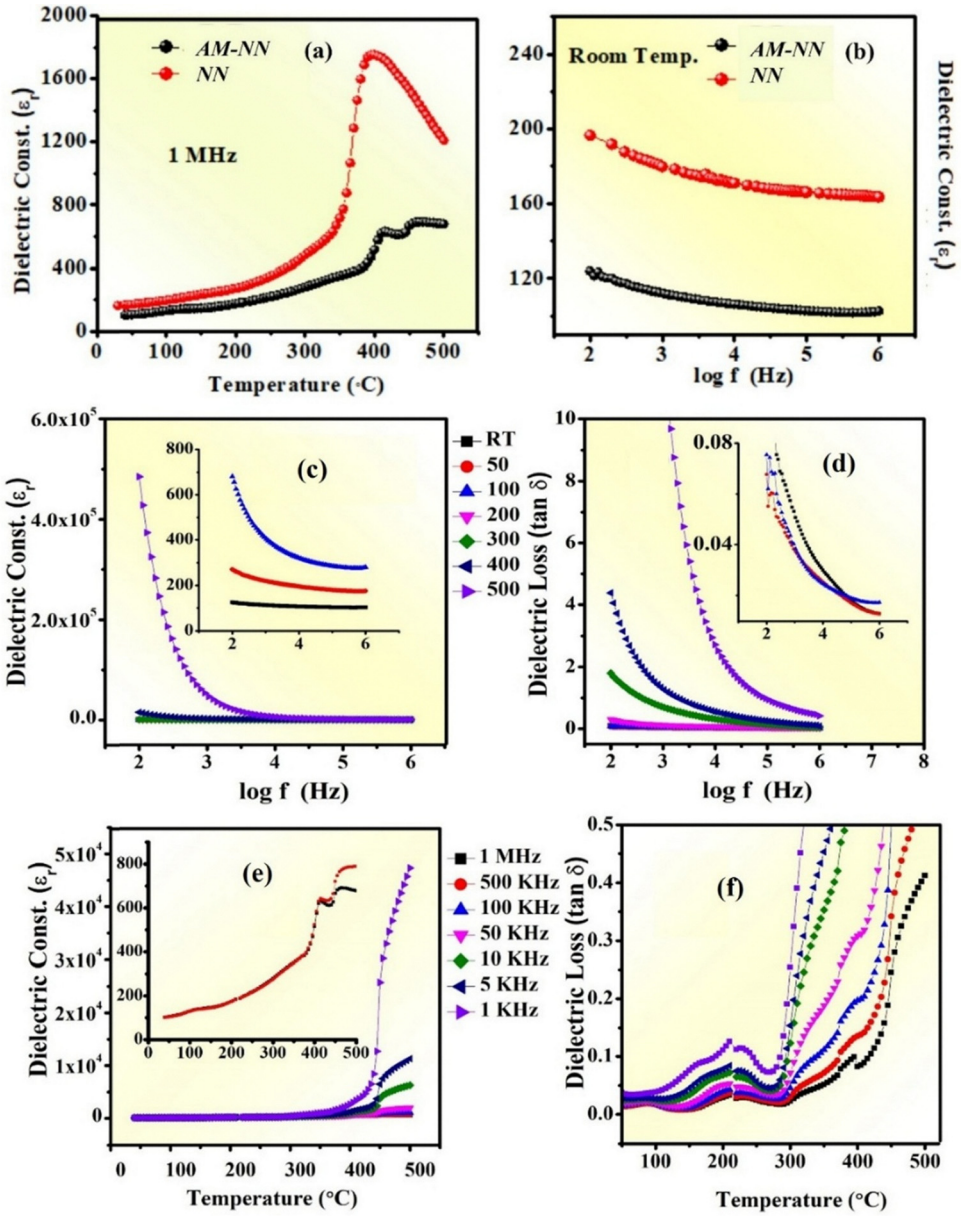

Fig. 4 (a) Temperature-dependent dielectric curve and (b) frequency-dependent dielectric curve of AM-NN and NN systems (c) frequency-dependent dielectric constant (d) dielectric loss at different temperatures (e) temperature-dependent dielectric constant (f) dielectric loss curve at different frequencies of AM-NN.

impedance, Y^* refers to the complex admittance, σ^* stands for the complex conductivity, and tan δ is the loss tangent.[48,53] The contributions from the bulk and grain boundaries can be separated and distinguished by analyzing the variations in the impedance response to an applied alternating field. Fig. 6(a) and (b) displays the complex impedance spectrum (Z' *vs.* Z'') for all the parent NN and AM-NN ceramics at a temperature range of 300 to 500 °C. A single semicircular arc for both indicates that the behavior is primarily due to the grain contribution, as the grain boundary typically exhibits higher resistance than the grain. This is because the grain boundary creates a potential barrier, which leads to an additional semicircle at lower frequencies.

The separation of grain and grain boundary effects is achieved by fitting the experimental data to an equivalent circuit model, typically represented by a parallel resistor–capacitor (R–C) element, as illustrated in the inset of Fig. 6(a) and (b). The mathematical representation of the circuit is as follows:

$$Z^* = \frac{1}{R^{-1} + i\omega C} = Z' - iZ''$$

Here, Z' and Z'' represent the real and imaginary components of the complex impedance, respectively. The fitting results closely match the measured data, revealing that the

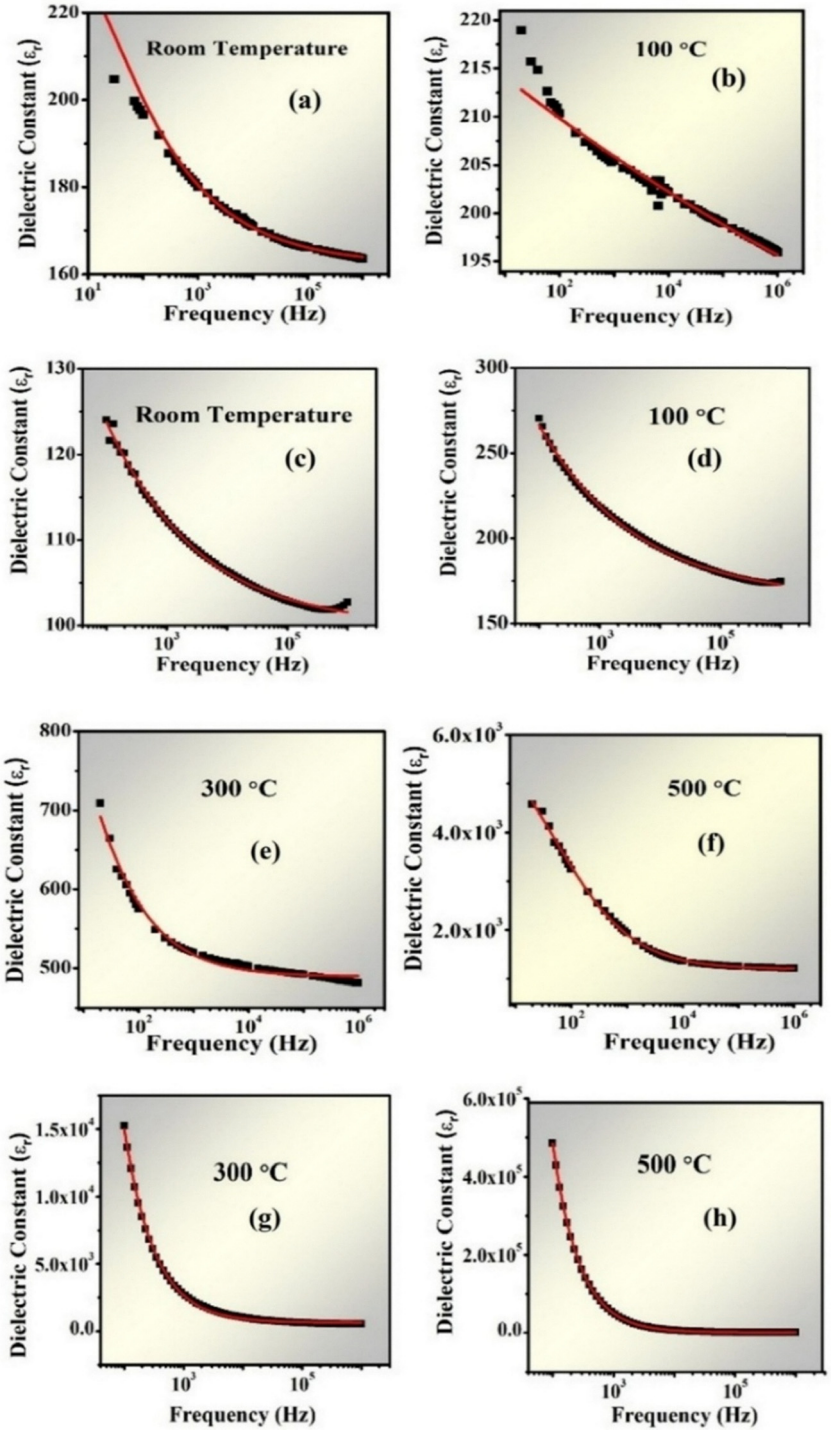

Fig. 5 Havriliak–Negami equation fitted to the frequency-dependent dielectric constant curve for NN (a), (b), (e) and (f) and AM-NN (c), (d), (g) and (h).

center of the semicircles is slightly shifted below the real axis (Z'). This shift is attributed to a distribution of relaxation times, which causes a deviation from the ideal Debye behavior. For non-Debye behavior, a constant phase element (CPE) is used in place of the capacitor (C).[54] The Cole–Cole plot shows tilted semicircular arcs, with the center positioned below the real axis, indicating a complex capacitance with a dissipative imaginary component. The angle of depression represents the phase angle of the capacitance at the frequency corresponding to the peak of the Cole–Cole plot, where $\omega R|C| = 1$.[54] The semicircular plots for the NN and AM-NN in ESI,† Fig. S3 are generated using Mathematica software. For the NN and AM-NN, the depressed angles are calculated to be 14.32° and 27.14° respectively. The increase in the depression angle in the AM-NN system indicates its non-Debye behavior. This non-Debye characteristic of the AM-NN system is further supported by

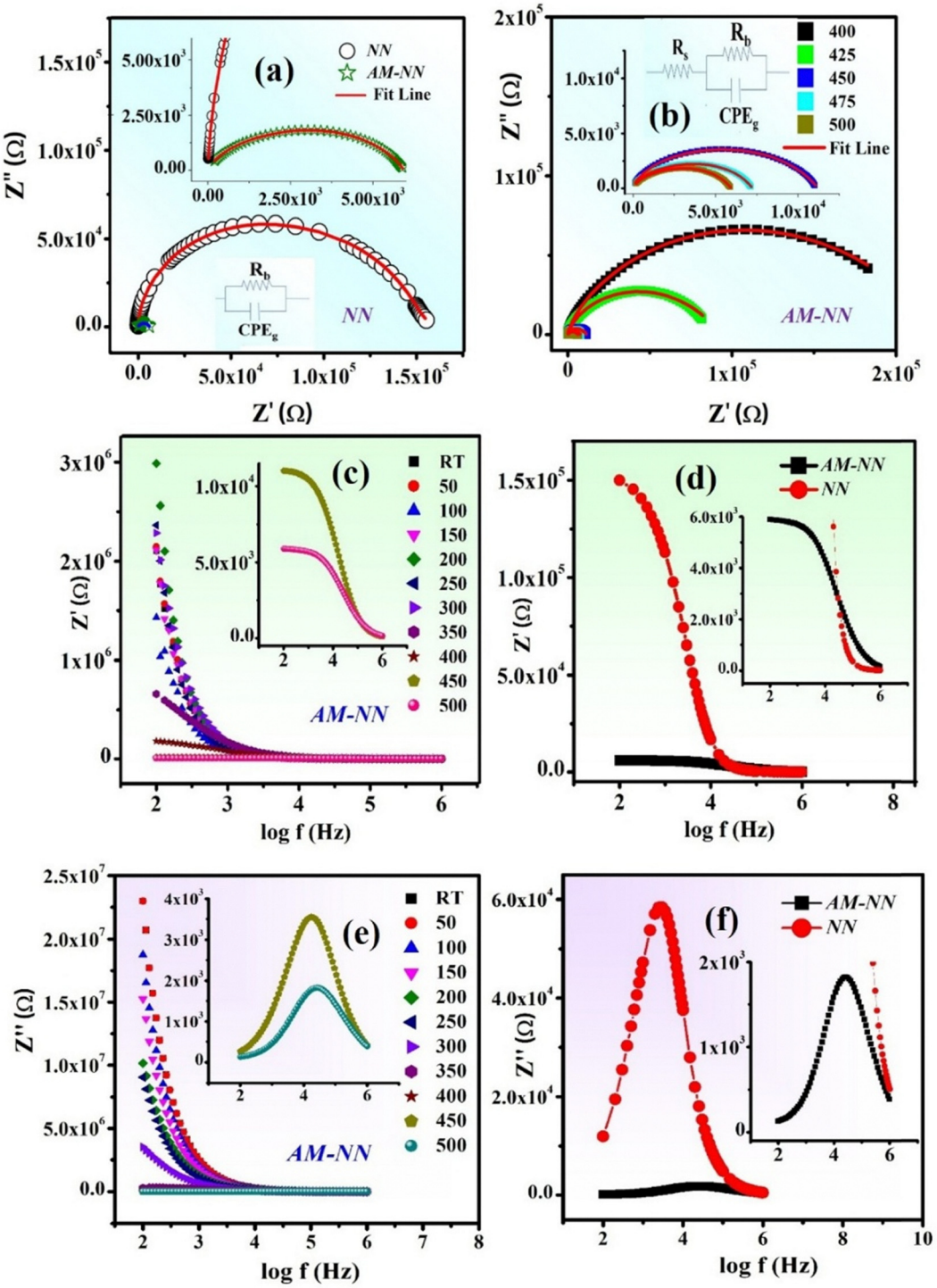

Fig. 6 (a) Comparative Cole–Cole plot of AM-NN and NN (inset is the circuit fitted to the Cole–Cole plot of NN) and (b) Cole–Cole plot of AM-NN at different temperatures ranging from 300 to 500 °C (inset is the circuit fitted to the Cole–Cole plot of AM-NN) (c) real impedance plot of AM-NN with frequency at different temperatures (d) comparative plot real impedance plot for NN and AM-NN (e) imaginary impedance plot of AM-NN with frequency at different temperatures (f) comparative plot real impedance plot for NN and AM-NN.

mathematical calculation, consistent with the explanation provided earlier. The variation of the real impedance (Z') of the AM-NN system with frequencies, ranging from 100 Hz to 1 MHz, at different temperatures, has been investigated as shown in Fig. 6(c). It is observed that the magnitude of Z' decreases with increasing frequency ($\log f$) as well as temperature (T), which suggests an increase in AC conductivity. Fig. 6(d) presents a comparative plot of the real impedance (Z') for NN and modified NN at 500 °C, highlighting an increase in AC conductivity in the Ag and Mg-modified AM-NN systems, which

is attributed to the presence of oxygen vacancies. The Z' values for all temperatures converge at high frequencies, which can be attributed to the release of space charge caused by the reduction in barrier properties as temperature increases.[55] This effect may also enhance AC conductivity with temperature at high frequencies. Additionally, at low frequencies, Z' values decrease with increasing temperature, displaying a negative temperature coefficient of resistance (NTCR) behavior, similar to that observed in semiconductors. Fig. 6(e) represents the imaginary impedance (Z'') plot of AM-NN as a function of frequency at different temperatures. Shifting of the Z'' peak to the higher temperature side suggests the occurrence of more than one relaxation process with increasing temperature and gives evidence of regarding the non-Debye type of relaxation process. Fig. 6(f) shows the comparative Z'' plot of AM-NN and NN advocating the non-Debye type nature of AM-NN as compared to $NaNbO_3$.[56]

3.7. Confirmation of oxygen vacancies through photoluminescence and UV-vis spectroscopy

The correlation between cationic modification and defects can change the electronic band structure of various materials, influencing properties such as photoluminescence, which are determined by electronic transition. When defects like vacancies, interstitials, or substitutional atoms are present, they introduce localized energy levels within the bandgaps. These levels can act as trap states for charge carriers, either enhancing or diminishing photoluminescence based on the characteristics of the defect. For example, some defects might create energy states that facilitate transitions from the conduction band to these traps, increasing photoluminescence. The photoluminescence emission bands are associated with different electronic transitions that are allowed between the energy levels created within the bandgap. For NN, the PL emission is particularly influenced by the local configuration of the NbO_6 octahedron. These structural factors are essential in shaping the energy levels and transitions that result in the observed luminescence. As Kröger–Vink notation describes, oxygen vacancies are among the most common defects in semiconductors and perovskite-oxide materials.[57] Teixeira *et al.*[29] in their report, mentioned that oxygen vacancies play a crucial role in the case of pristine NN and show PL activities, which are generally observed in the case of rare earth element-modified systems. In Fig. 7(a) and (b) PL spectra of NN and AM-NN are presented and a significant hump at 610 nm is observed for both systems' suggesting the presence of oxygen vacancies as

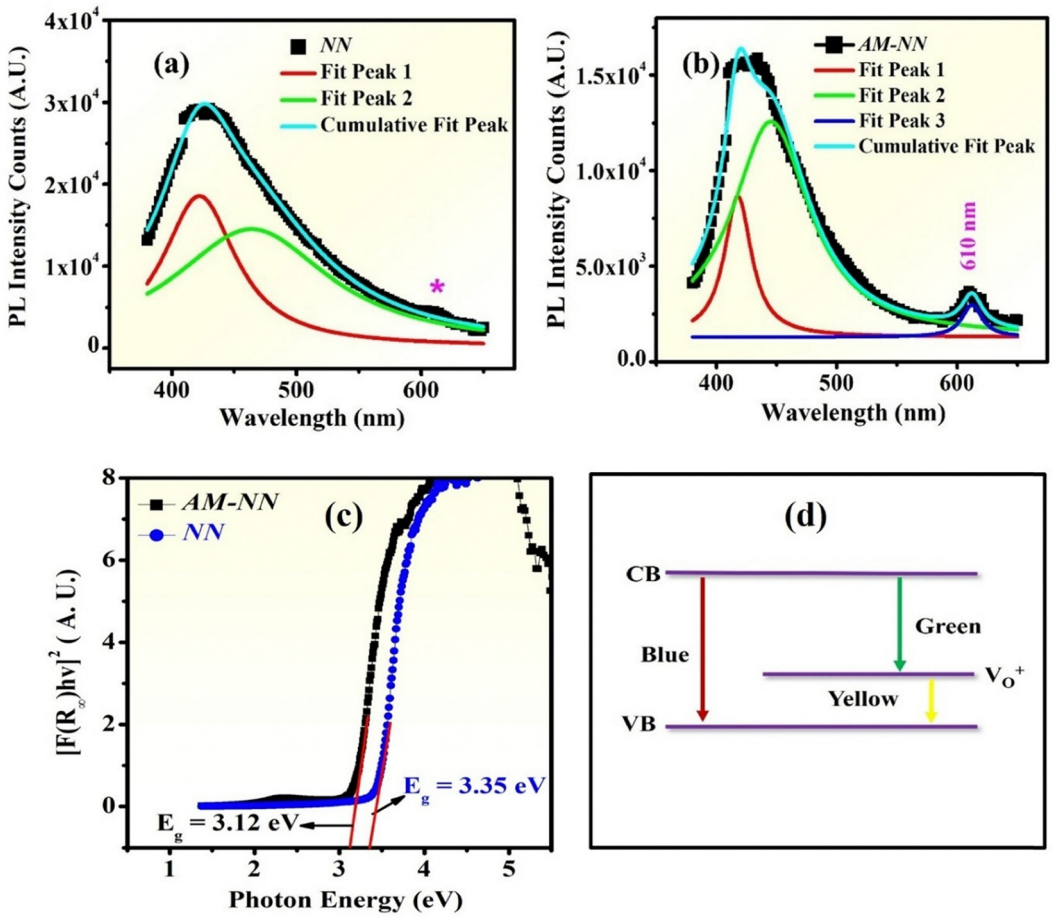

Fig. 7 Deconvoluted PL spectra of (a) NN (b) AM-NN systems (c) UV-vis spectra of NN and AM-NN (d) schematic diagram of different bands in the modified system.

mentioned in the literature earlier. In the modified AM-NN system the hump at 610 nm is prominently indicating the enhanced involvement of oxygen vacancies in the case of the modified system. AgO as the raw material is not stable by nature and stabilizes as Ag_2O, generating more oxygen vacancies as represented in the below equation using Kröger–Vink notation.

$$2AgO \rightarrow Ag_2O + \frac{1}{2}O_2$$

$$\left[Ag_2O \cdot V_O^{\times}\right] \rightarrow \left[Ag_2O \cdot V_O^{\bullet}\right]$$

$$\left[Ag_2O \cdot V_O^{\bullet}\right] \rightarrow \left[Ag_2O \cdot V_O^{\bullet\bullet}\right]$$

An increase in oxygen vacancies contributes to medium-range structural disorder, leading to a narrowing of the optical band gap. The resulting structural disorder is reflected in the broad PL band profile, where the hump associated with structural defects becomes prominent in the modified system. This suggests that shallow energy levels have formed within the band gap. Consequently, the density of these shallow levels is greater in the modified NN due to the presence of these vacancies. Fig. 7(a) and (b) illustrates the photoluminescence (PL) spectra of NN and modified AM-NN at ambient temperature. Both samples exhibit broad emission bands ranging from 350 to 750 nm, and the peak of these bands is located around 420 nm. However, the emission intensity is lower in the AM-NN compared to the NN. The broad-band photoluminescence (PL) emission shown in Fig. 7(d) is typical of a mechanism where the band gap is relaxed between intermediary levels.

The observed differences in the PL band profiles, including variations in intensity and broadening, are attributed to changes in the band gap energy (E_{gap}) due to the modification. The PL emission typically exhibits a broad band profile for many semiconductors and perovskite-based materials.[29] Fig. 7(c) shows the UV-vis spectrum of NN and AM-NN and the band gap determined for both systems is found to be 3.35 eV and 3.12 eV respectively. The decreased band gap in the modified system may be due to the presence of oxygen vacancies and the reduced band gap enhances the photocatalytic behavior of the systems.[58] Therefore, after getting the bandgap, we performed the photocatalytic analysis of the sample. The reduced band gap in Fig. 7(c) reflects a mechanism in which an intermediary level relaxes the band gap. An additional intermediate metastable state is created between the conduction and valence bands due to the presence of oxygen vacancies, as illustrated schematically in Fig. 7(d).

3.8. Dipole and defect-driven photocatalytic properties in AM-NN systems

The photocatalytic activity of NN and AM-NN, shown in Fig. S4 and S5 (ESI†), presents the absorbance spectra of dyes such as RhB, CV, CR, and MB in the presence of the catalyst, measured at various time intervals under visible light exposure. From the above figures, it is clear that the absorbance of RhB, CV, CR, and MB consistently decreases over time with irradiation.

The maximum absorbance is observed at 544, 588, 498, and 644 nm for each dye, respectively. The intensity of these absorption peaks is directly associated with the color ratio to the solution. Next, we investigated the photocatalytic performance of NN and AM-NN in the degradation of these dyes under tungsten lamp exposure. The below-mentioned equation is used to calculate the percentage degradation of the organic dyes:[59,60]

$$\text{Degradation rate } (\eta) = \frac{C_0 - C_t}{C_0} \times 100\%$$

where C_t represents the concentration of the dye solution at time t, and C_0 is the initial concentration at time $t = 0$. Fig. 8(a) shows that AM-NN demonstrated excellent photocatalytic activity as compared to NN. Degradation efficiency for NN and AM-NN in the case of MB and CV dyes are around 94% and 99%, respectively, within 5 h, which is quite similar for both the systems. But in the case of CR and RhB, the degradation efficiency of AM-NN (*i.e.* 60% for CR and 20% for RhB) is higher than NN (*i.e.* 5% for CR and 5% for RhB) within 5 h as shown in Fig. 8(a). The difference in degradation efficiencies of various dyes for the same catalyst has been previously reported by Saha *et al.*[61,62] This variation could be attributed to several factors. One factor is the differing abilities of the dyes to inject electrons in the conduction band of the photocatalyst.

Additionally, the chemical structure of the organic dyes plays a significant role in their reactivity during the photocatalytic degradation process. Organic dye molecules typically contain varying numbers of functional groups, which can lead to different reactions and the formation of various intermediate products, ultimately influencing the degradation efficiency. AgO as the raw material contributing towards the creation of oxygen vacancies results in the decrease in the band gap of modified NN. This allows the material to absorb visible light more effectively, enhancing its photocatalytic activity. Oxygen vacancies contribute to a higher charge density within the material. This increase facilitates better charge separation and transfer during photocatalytic reactions, which is crucial for efficient photocatalysis.[61] As depicted in Fig. 8(a) the AM-NN shows a notable increase in photodegradation efficiency compared to pure NN. The kinetic rate constants were determined by fitting the experimental data points to a pseudo-first-order kinetic model. The photodegradation rate was studied by adding 50 mg of photocatalysts to a 50 ml solution of MB, CV, CR, and RhB (10 ppm) in a beaker. The suspension was stirred in the dark for 60 minutes to reach adsorption–desorption equilibrium, after which it was exposed to visible light irradiation from a tungsten lamp. The linear fit indicates that the dye degradation process follows the pseudo-first-order model, as shown below:[60]

$$-\frac{dC}{dt} = kC$$

$$\Rightarrow -\ln\frac{C_t}{C_0} = kt$$

The reaction rate constant, denoted as k, is determined by analyzing the slope of a plot as shown in Fig. 9(c), (d), (g) and (h).

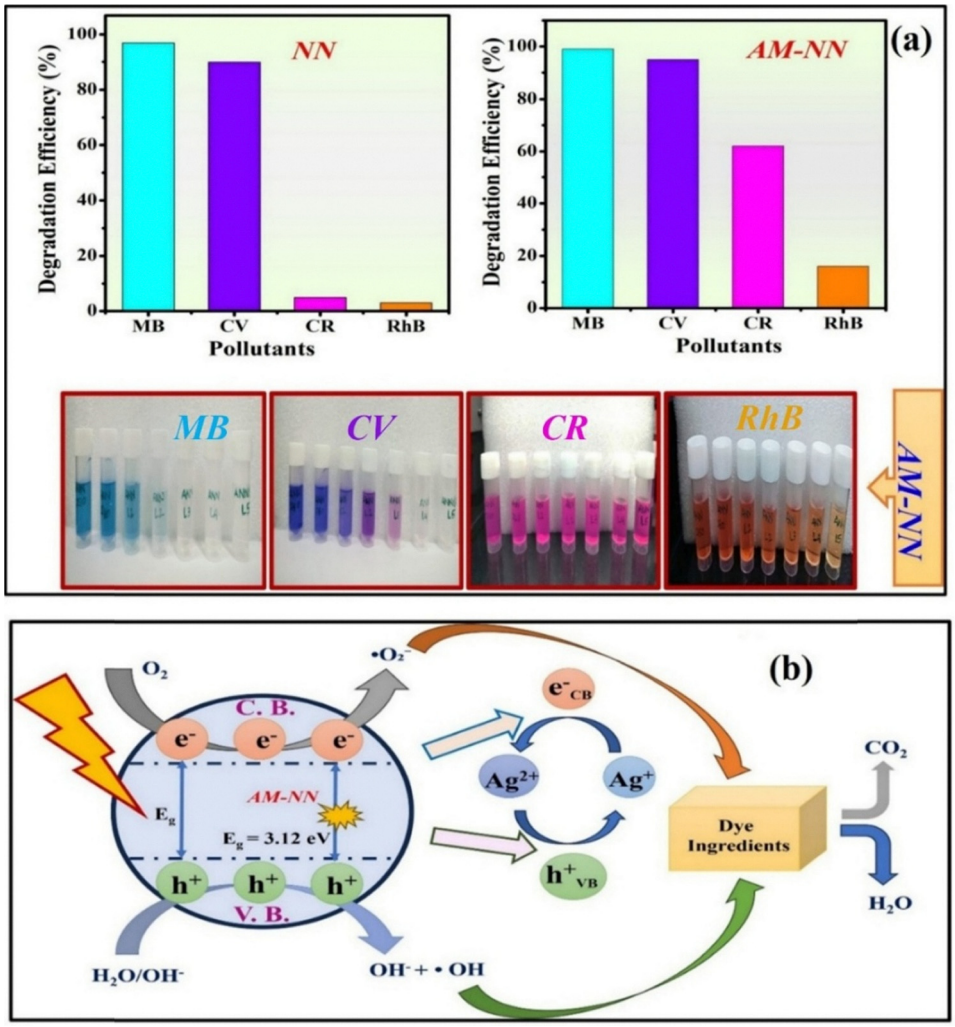

Fig. 8 (a) Degradation efficiency of NN and AM-NN for different dyes (b) schematic diagram representing the degradation process of dye.

The estimated values of k at t = 300 minutes are provided in the ESI.† The values for k are 0.0005, 0.0027, 0.0138, and 0.0128 min^{-1} for RhB, CR, CV, and MB dyes, respectively which is higher than that of the parent NN. The findings of this study indicate that the AM-NN material holds promise as a perovskite photocatalyst for the efficient removal of organic dyes from solutions.

To elucidate the reactive species responsible for photocatalytic dye degradation under solar irradiation, selective radical scavengers were employed to quench specific active species. A systematic scavenging study utilized disodium ethylenediaminetetraacetate (EDTA) for photogenerated hole (h^+) capture, ethanol (EtOH) for hydroxyl radical ($OH^\bullet$) quenching, and 1,4-benzoquinone (*p*-BQ) for superoxide radical ($O_2^{\bullet -}$) trapping. The scavenger dosages were optimized at 1 mM EDTA, 2 mM EtOH, and 1 mM *p*-BQ, with photodegradation performance evaluated through normalized concentration ratios (C_t/C_0) as depicted in Fig. 10(a) for methylene blue (MB). The reaction rate constant, denoted as k, is determined by analyzing the slope of a plot as shown in Fig. 10(b).

The experimental results, as presented in Fig. 10(c), demonstrate substantial inhibition of the photocatalytic process compared to the reference system without scavengers when EtOH and EDTA were introduced, confirming the crucial roles of $OH^\bullet$ radicals and photogenerated holes in the degradation mechanism of MB. Specifically, EtOH addition resulted in a dramatic decrease in MB degradation efficiency from 99% to 30%. Similarly, EDTA incorporation caused a significant reduction in degradation performance from 99% to 46% for MB. Conversely, *p*-BQ addition produced only marginal inhibition, with MB degradation efficiency decreasing modestly to 94%, suggesting that superoxide radicals play a minor role in the overall photodegradation pathway.

Based on the above scavenger results, a possible mechanism for the AM-NN with improved activity is proposed. To activate the photocatalytic process, the photocatalyst must absorb light photons with energy equal to or greater than its band gap. This absorption excites electrons in the valence band, causing them to move to the conduction band, thus generating charge carriers. As represented in the Fig. 8(b) when the AM-NN particles are exposed to visible light, the photo-induced electrons interact with oxygen molecules (O_2) on the catalyst surface, leading to the formation of superoxide radicals ($^\bullet O_2^-$).

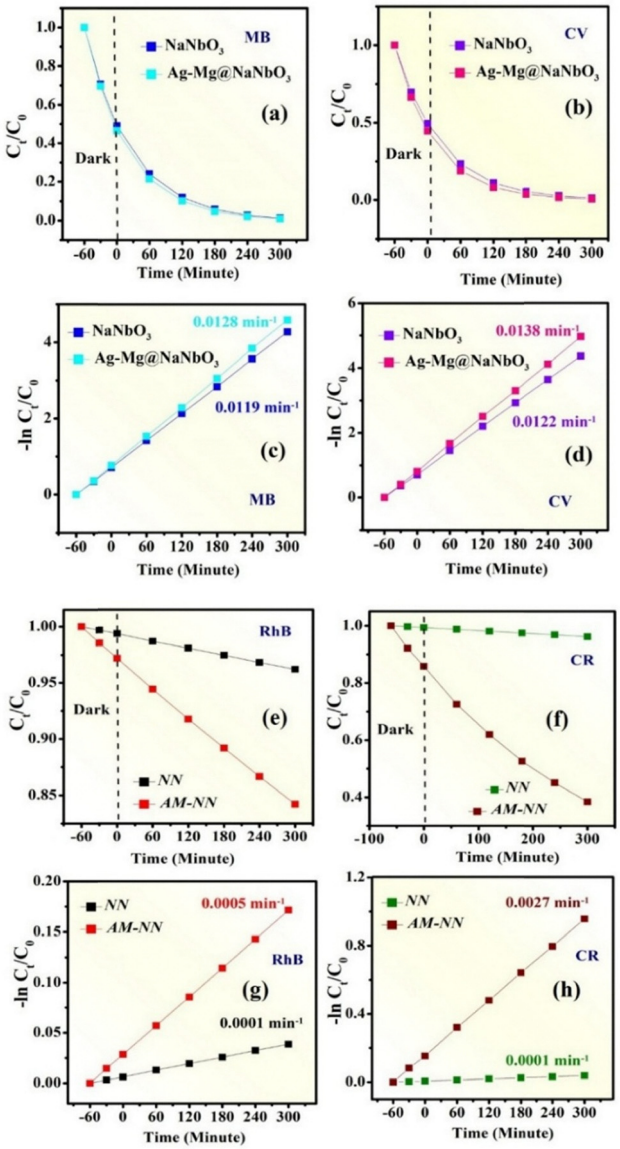

Fig. 9 (a) and (b) Plot showing the concentration (c) and (d) pseudo first order kinetics plot of MB and CV of NN and AM-NN. (e) and (f) Plot showing the concentration (g) and (h) pseudo first order kinetics plot of RhB and CR of NN and AM-NN.

As we have used AgO as the raw material the concentration of superoxide radicals ($^{\bullet}O_2^-$) will be higher than usual. Simultaneously, the photo-induced holes interact with water molecules (H_2O) at the catalyst surface, producing hydroxyl radicals ($^{\bullet}OH$). These reactive species then participate in the degradation reactions. The reactions involving superoxide radicals ($^{\bullet}O_2^-$) and water molecules (H_2O) lead to the formation of hydrogen peroxide (H_2O_2). Under light exposure, hydrogen peroxide decomposes into hydroxyl radicals ($^{\bullet}OH$). These hydroxyl radicals are highly reactive and play a crucial role in breaking down organic pollutants into harmless byproducts like carbon dioxide and water. The efficiency of photocatalytic degradation for a particular dye is influenced by the compatibility between the energy levels of the excited dye and the conduction band of the photocatalyst. This interaction determines the overall degradation rate for specific dyes. The photocatalytic process can be described by the following equation:

$$Na_{0.85}Ag_{0.15}Nb_{0.95}Mg_{0.05} + h\nu \rightarrow Na_{0.85}Ag_{0.15}Nb_{0.95}Mg_{0.05}\,(e_{cb}^- + h_{vb}^+)$$

$$h_{vb}^+ + H_2O \rightarrow {}^{\bullet}OH + H^+$$

$$^{\bullet}OH + \text{dye} \rightarrow H_2O + CO_2 + \text{products due to degradation of dye}$$

$$e_{cb}^- + O_2 \rightarrow {}^{\bullet}O_2^-$$

$$^{\bullet}O_2^- + H_2O \rightarrow OH^- + {}^{\bullet}HO_2$$

$$^{\bullet}HO_2 + H_2O \rightarrow H_2O_2 + {}^{\bullet}OH$$

$$H_2O_2 + e_{cb}^- \rightarrow OH^- + {}^{\bullet}OH$$

$$^{\bullet}OH + \text{dye} \rightarrow H_2O + CO_2 + \text{products due to degradation of dye}$$

Fig. 9(a) and (b) illustrates the variation in relative concentration (C_t/C_0) of different dye solutions as time progresses. Fig. 8(a) presents the photocatalytic activity of AM-NN in the degradation of these dye solutions. In case ferroelectric dipoles are present in the system, this facilitates the generation of several holes and electrons, which will enhance the photocatalytic process as presented in the schematic diagram Fig. S6(a) (ESI†). After using the sample of AM-NN in dye degradation, we performed the XRD of the used sample. The comparative XRD graph as shown in Fig. S6(b) (ESI†) of the used and unused samples suggests that there are no extra peaks obtained for the used sample. This suggests the reusability of the AM-NN system for dye degradation for several cycles.

3.9. Exploring oxygen vacancies' effects on photoelectrochemical behaviour in AM-NN system

Photoelectrochemical measurements (PEC) were conducted in a neutral electrolyte solution (0.1 M Na_2SO_4) at pH 7. The photocurrent density was recorded in a quartz glass beaker using a standard three-electrode setup. Ag/AgCl served as the reference electrode, Pt was used as the counter electrode, and the desired samples were coated on the third working electrode. The electrochemical impedance spectroscopy (EIS) experiment was conducted with a sinusoidal perturbation of 5 mV amplitude, over a frequency range from 100 kHz to 0.1 Hz. The schematic diagram of the whole setup is shown in Fig. 11(a). To convert the measured applied potential *versus* Ag/AgCl into the potential relative to the reversible hydrogen electrode (RHE), the Nernst equation was used:

$$E_{RHE} = E_{Ag/AgCl} + E^0_{Ag/AgCl} + (59\ \text{mV})\cdot\text{pH}$$

In this equation, $E^0_{Ag/AgCl}$ is the standard electrode potential of Ag/AgCl (0.1976 V) at 25 °C, and the pH was set to 7.

PEC will provide further information regarding charge transfer and light sensitivity. As shown in Fig. 11(b), the

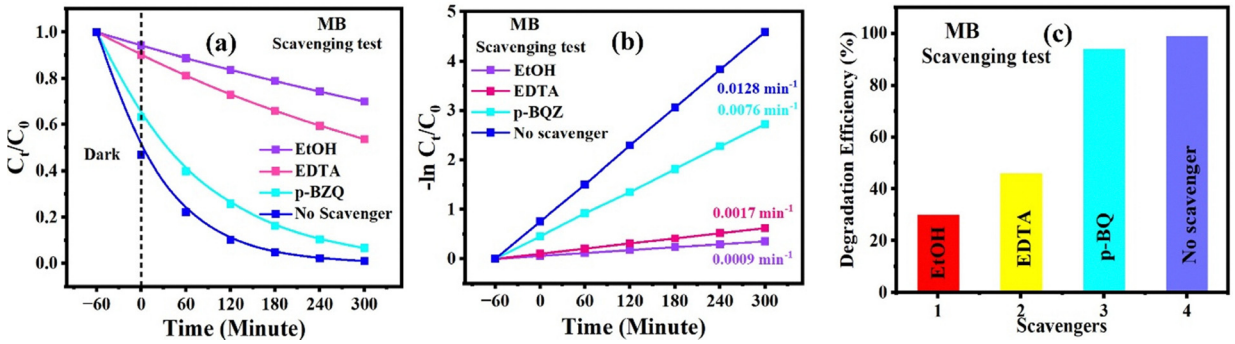

Fig. 10 (a) Plot showing the concentration (b) pseudo first order kinetics plot of MB and (c) degradation efficiency of MB scavenging test.

photocurrent density of AM-NN is higher than the NN, suggesting its superior photo activity. For both modified and parent NN, dark photocurrent density is lower than light condition owing to its photoactive behavior.[63–65] PEC water splitting showed that the photoanode fabricated with AM-NN exhibits enriched photocurrent density (1.11 mA cm^{-2}). The theoretical electrochemical circuit fitted in Fig. 11(c) depicts that the R_{CT} (charge transfer resistance) of NN and AM-NN were 5721.8 Ω and 1115.3 Ω, respectively. The lower charge transfer resistance corresponds to efficient charge transfer, which means there is

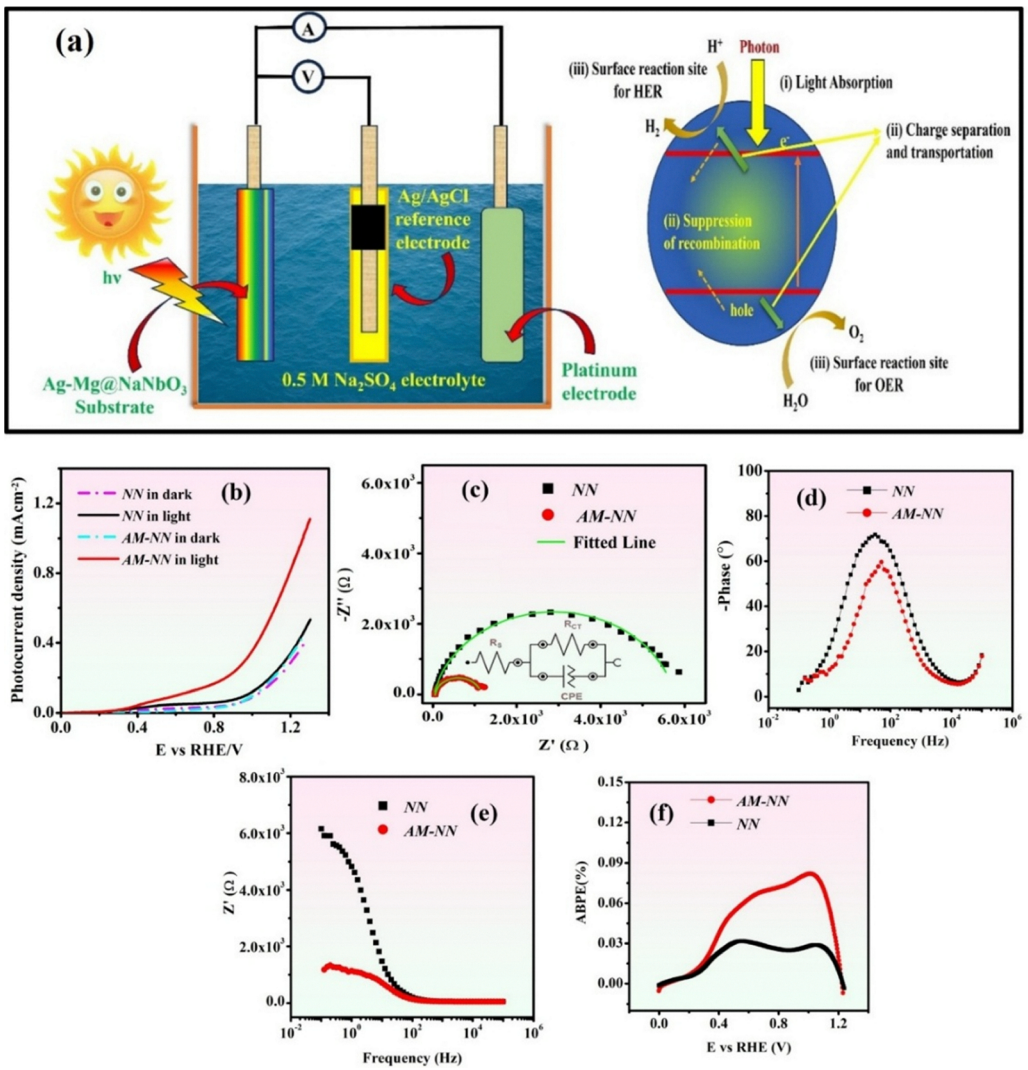

Fig. 11 (a) Schematic diagram of the whole PEC system and mechanism behind the PEC. (b) Photocurrent density plot (c) electrochemical impedance spectra (d) Bode phase plot (e) real impedance spectra for NN and AM-NN (f) ABPE as a function of applied potential *versus* RHE.

Table 3 Electrochemical impedance data fitting parameters of the NN and AM-NN photoelectrode

Sample	R_S (Ohm)	R_{ct} (Ohm)	CPE (Farad)
NN	31.766	5721.8	1.15×10^{-5}
AM-NN	53.021	1115.3	1.66×10^{-5}

an efficient charge transfer occurring in AM-NN. The fitted parameters are displayed in Table 3, revealing the enhanced property of AM-NN due to oxygen vacancies. The bode phase diagram acquired from EIS spectra is shown in Fig. 11(d). The lower phase angle and frequency maxima correspond to a higher electron lifetime in the circuit. The NN and AM-NN system has shown an improved lifetime of the photoexcited electron. Fig. 11(e) shows the real impedance *vs.* frequency graph of NN and AM-NN, suggesting a decrease in resistivity with the modification of Ag and Mg.

The applied bias photon to the current efficiencies (ABPE) for various photoanodes-based NN and AM-NN were determined from the below-mentioned equation:

$$\text{ABPE}\ (\%) = \left(\frac{I \times \left(1.23 - V_{\text{app}}\right)}{P_{\text{incident}}}\right) \times 100\%$$

Here, V_{app} represents the external applied potential relative to RHE, I denote the measured current density, and P_{incident} refers to the power density of the incoming light (mW cm^{-2}).

As illustrated in Fig. 11(f), the AM-NN photoanode achieves a peak efficiency of approximately 0.08% (at 1.013 V *vs.* RHE) which is about 4 times higher than that of pure NN (0.02% at 1.045 V *vs.* RHE) photoanode. The %ABPE result obtained for our system closely resembles the findings reported for ZnO-based materials by Koyale *et al.*[66] and Liu *et al.*[67] The PEC results are consistent with the complex impedance spectroscopy findings, which confirm the reliability of the outcome.

4. Conclusion

A lead-free, oxygen vacancy generated AM-NN ferroelectric material was synthesized *via* a solid-state method. Comparative Raman analysis of both NN and AM-NN confirmed the formation of oxygen vacancies in the modified system. The influence of these vacancies on the dielectric properties was investigated using theoretical models. The resistance and capacitance of the materials were measured using complex impedance spectroscopy. The derived data from the impedance data indicated the presence of oxygen vacancies in the AM-NN system due to the addition of AgO and MgO. Photoluminescence spectroscopy further supported the presence of oxygen vacancies, as evidenced by an additional peak. UV-Vis spectroscopy determined the bandgap of the AM-NN system to be 3.12 eV, making it suitable for photocatalytic applications. The AM-NN exhibited approximately 90% efficiency for MB and CV dyes and around 60% efficiency for CR. X-ray diffraction analysis of the used sample showed no extra peaks, indicating the material's reusability. The water splitting performance, quantified by the ABPE (%), demonstrated that the AM-NN system performed similarly to well-known photocatalysts, such as ZnO. Overall, the strategic introduction of oxygen vacancies in the AM-NN system enhanced its conductivity, as well as photocatalytic efficiency, and reduced its bandgap, making it suitable for a variety of photocatalytic applications.

Author contributions

A. Singha: conceptualization, methodology, validation, formal analysis, investigations, writing – original draft. M. Kumar: investigation of photocatalytic, review & editing the part. P. P. Cho: validation, investigation of photocatalytic, review & editing the part. S. Challapalli: validation, resources, review & editing. S. Lavadiya: investigation of PL. S. S. K. Raavi: validation, resources, review & editing. S. Asthana: conceptualization, review & editing, visualization, validation, supervision, resources, project administration, funding acquisition.

Conflicts of interest

The authors declare no competing financial interest.

Ethical approval

The manuscript reflects the author's own research and analysis truthfully and completely. We expressly declare that all ethical rules are followed during the experiments and the process of converting the work into a manuscript.

Data availability

The data supporting this article have been included as part of the ESI.†

Acknowledgements

Author AS would like to extend her heartfelt gratitude to the Indian Institute of Technology Hyderabad (IITH) for providing financial support through the IITH-IPDF program.

References

1 S. T. Ong, P. S. Keng, W. N. Lee, S. T. Ha and Y. T. Hung, Dye waste treatment, *Water*, 2011, **3**(1), 157–176, DOI: 10.3390/w3010157.
2 Y. Cui, J. Briscoe and S. Dunn, Effect of ferroelectricity on solar-light-driven photocatalytic activity of $BaTiO_3$: Influence on the carrier separation and Stern layer formation, *Chem. Mater.*, 2013, **25**(21), 4215–4223, DOI: 10.1021/cm402092f.
3 I. K. Konstantinou and T. A. Albanis, TiO_3-assisted photocatalytic degradation of azo dyes in aqueous solution: kinetic and mechanistic investigations: a review, *Appl. Catal., B*, 2004, **49**(1), 1–14, DOI: 10.1016/j.apcatb.2003.11.010.
4 A. Rafiq, M. Ikram, S. Ali, F. Niaz, M. Khan, Q. Khan and M. Maqbool, Photocatalytic degradation of dyes using

semiconductor photocatalysts to clean industrial water pollution, *J. Ind. Eng. Chem.*, 2021, **97**, 111–128, DOI: 10.1016/j.jiec.2021.02.017.

5 S. Assavachin and F. E. Osterloh, Ferroelectric polarization in $BaTiO_3$ nanocrystals controls photoelectrochemical water oxidation and photocatalytic hydrogen evolution, *J. Am. Chem. Soc.*, 2023, **145**(34), 18825–18833, DOI: 10.1021/jacs.3c03762.

6 Y. Wang, X. Sun, J. Ma, Z. Yi, S. Wang, G. Liu and H. Yang, Coupled piezo-pyro-photocatalysis of oxygen vacancies and Bi quantum dots co-modified $BaTiO_3$ for highly efficient removal of ciprofloxacin, *Sep. Purif. Technol.*, 2024, **337**, 126392, DOI: 10.1016/j.seppur.2024.126392.

7 J. M. Herrmann, Heterogeneous photocatalysis: fundamentals and applications to the removal of various types of aqueous pollutants, *Catal. Today*, 1999, **53**(1), 115–129, DOI: 10.1016/S0920-5861(99)00107-8.

8 R. Shrestha, S. Ban, S. Devkota, S. Sharma, R. Joshi and A. P. Tiwari, *et al.*, Technological trends in heavy metals removal from industrial wastewater: A review, *J. Environ. Chem. Eng.*, 2021, **9**(4), 105688, DOI: 10.1016/j.jece.2021.105688.

9 C. Bertoni, D. Gallardo, S. Dunn, N. Gaponik and A. Eychmüller, Fabrication and characterization of red-emitting electroluminescent devices based on thiol-stabilized semiconductor nanocrystals, *Appl. Phys. Lett.*, 2007, **90**(3), 034107, DOI: 10.1063/1.2433030.

10 A. Harhira, L. Guilbert, P. Bourson and H. Rinnert, Decay time of polaron photoluminescence in congruent lithium niobate, *Phys. Status Solidi C*, 2007, **4**(3), 926–929, DOI: 10.1002/pssc.200673755.

11 N. J. Bell, Y. H. Ng, A. Du, H. Coster, S. C. Smith and R. Amal, Understanding the enhancement in photoelectrochemical properties of photocatalytically prepared TiO_3-reduced graphene oxide composite, *J. Phys. Chem. C*, 2011, **115**(13), 6004–6009, DOI: 10.1021/jp1113575.

12 M. Stock and S. Dunn, $LiNbO_3$ – A new material for artificial photosynthesis, *IEEE Trans. Ultrason. Ferroelectr. Freq. Control*, 2011, **58**(9), 1988–1993, DOI: 10.1109/TUFFC.2011.2042.

13 Y. Guo, K. I. Kakimoto and H. Ohsato, Phase transitional behavior and piezoelectric properties of (Na0.5K0.5)NbO3–LiNbO3 ceramics, *Appl. Phys. Lett.*, 2004, **85**(18), 4121–4123, DOI: 10.1063/1.1813636.

14 F. Dutto, C. Raillon, K. Schenk and A. Radenovic, Nonlinear optical response in single alkaline niobate nanowires, *Nano Lett.*, 2011, **11**(6), 2517–2521, DOI: 10.1021/nl201085b.

15 S. Kim, J. H. Lee, J. Lee, S. W. Kim, M. H. Kim and S. Park, *et al.*, Synthesis of monoclinic potassium niobate nanowires that are stable at room temperature, *J. Am. Chem. Soc.*, 2013, **135**(1), 6–9, DOI: 10.1021/ja308209m.

16 Q. Liu, Y. Chai, L. Zhang, J. Ren and W. L. Dai, Highly efficient $Pt/NaNbO_3$ nanowire photocatalyst: its morphology effect and application in water purification and H_2 production, *Appl. Catal., B*, 2017, **205**, 505–513, DOI: 10.1016/j.apcatb.2016.12.065.

17 L. Yan, T. Zhang, W. Lei, Q. Xu, X. Zhou and P. Xu, *et al.*, Catalytic activity of gold nanoparticles supported on $KNbO_3$ microcubes, *Catal. Today*, 2014, **224**, 140–146, DOI: 10.1016/j.cattod.2013.11.033.

18 A. K. Dhanka, M. Tiwari, P. K. Bhartiya, B. Pani, N. Agasti and D. Mishra, Oxygen vacancies induced low overpotentials of Ag/CeO_2 for electrocatalytic evolution of oxygen and hydrogen, *Mater. Adv.*, 2025, **6**(11), 3716–3729, DOI: 10.1039/d5ma00321k.

19 M. N. Alabdulsalam and A. A. Bagabas, Silver nanoparticles-promoted bismuth titanate perovskite nanosheets photocatalyst for water purification, *Results Chem.*, 2024, **10**, 101725, DOI: 10.1016/j.rechem.2024.101725.

20 B. Matović, J. M. Luković, B. Stojadinović, S. Aškrabić, A. R. Zarubica and B. M. Babić, *et al.*, Influence of Mg doping on structural, optical and photocatalytic performances of ceria nanopowders, *Process. Appl. Ceram.*, 2017, **11**(4), 304–310, DOI: 10.2298/pac1704304m.

21 J. Carrasco, N. Lopez and F. Illas, First principles analysis of the stability and diffusion of oxygen vacancies in metal oxides, *Phys. Rev. Lett.*, 2004, **93**(22), 225502, DOI: 10.1103/PhysRevLett.93.225502.

22 L. Di, H. Yang, T. Xian and X. Chen, Enhanced photocatalytic activity of $NaBH_4$ reduced $BiFeO_3$ nanoparticles for rhodamine B decolorization, *Materials*, 2017, **10**(10), 1118, DOI: 10.3390/ma10101118.

23 M. Hu, Q. Zhu, Y. Zhao, G. Zhang, C. Zou and O. Prezhdo, *et al.*, Facile removal of bulk oxygen vacancy defects in metal oxides driven by hydrogen-dopant evaporation, *J. Phys. Chem. Lett.*, 2021, **12**(39), 9579–9583, DOI: 10.1021/acs.jpclett.1c02687.

24 F. Gunkel, D. V. Christensen, Y. Z. Chen and N. Pryds, Oxygen vacancies: the (in)visible friend of oxide electronics, *Appl. Phys. Lett.*, 2020, **116**(12), 120505, DOI: 10.1063/1.5143309.

25 G. Cilaveni, K. A. Kumar, S. S. K. Raavi, C. Subrahmanyam and S. Asthana, Control over relaxor, piezo-photocatalytic and energy storage properties in $Na_{0.5}Bi_{0.5}TiO_3$ *via* processing methodologies, *J. Alloys Compd.*, 2019, **798**, 540–552, DOI: 10.1016/j.jallcom.2019.05.235.

26 C. Goutham, K. V. A. Kumar, S. S. K. Raavi, C. Subrahmanyam and S. Asthana, Enhanced electrical and photocatalytic activities in $Na_{0.5}Bi_{0.5}TiO_3$ through structural modulation by using anatase and rutile phases of TiO_3, *J. Materiomics*, 2022, **8**(1), 18–29, DOI: 10.1016/j.jmat.2021.06.003.

27 J. Rodríguez-Carvajal, Recent advances in magnetic structure determination by neutron powder diffraction, *Phys. B*, 1993, **192**(1–2), 55–69, DOI: 10.1016/0921-4526(93)90108-I.

28 R. Mouta, R. X. Silva and C. W. A. Paschoal, Tolerance factor for pyrochlores and related structures, *Acta Crystallogr., Sect. B: Struct. Sci., Cryst. Eng. Mater.*, 2013, **69**(5), 439–445, DOI: 10.1107/S2052519213020514.

29 G. F. Teixeira, E. S. Junior, A. Z. Simões, E. Longo and M. A. Zaghete, Unveiling the correlation between structural order-disorder character and photoluminescence emissions of $NaNbO_3$, *CrystEngComm*, 2017, **19**(30), 4378–4392, DOI: 10.1039/C7CE00218A.

30 K. A. Aly, N. M. Khalil, Y. Algamal and Q. M. Saleem, Lattice strain estimation for $CoAl_2O_4$ nanoparticles using Williamson-Hall analysis, *J. Alloys Compd.*, 2016, **676**, 606–612, DOI: 10.1016/j.jallcom.2016.03.213.

31 K. E. Johnston, C. C. Tang, J. E. Parker, K. S. Knight, P. Lightfoot and S. E. Ashbrook, The polar phase of $NaNbO_3$: a combined study by powder diffraction, solid-state NMR, and first-principles calculations, *J. Am. Chem. Soc.*, 2010, **132**(25), 8732–8746, DOI: 10.1021/ja101860r.

32 Y. Lu, T. Karaki and T. Fujii, Hydrothermal synthesis of plate-like sodium niobate particles, *Ceram. Int.*, 2015, **41**(Suppl. 1), S174–S179, DOI: 10.1016/j.ceramint.2015.03.231.

33 Y. D. Juang, S. B. Dai, Y. C. Wang, W. Y. Chou, J. S. Hwang and M. L. Hu, *et al.*, Phase transition of $LixNa_{1-x}NbO_3$ studied by Raman scattering method, *Solid State Commun.*, 1999, **111**(12), 723–728, DOI: 10.1016/S0038-1098(99)00232-X.

34 A. J. Paula, M. A. Zaghete, E. Longo and J. A. Varela, Microwave-assisted hydrothermal synthesis of structurally and morphologically controlled sodium niobates by using niobic acid as a precursor, *Eur. J. Inorg. Chem.*, 2008, 1300–1308, DOI: 10.1002/ejic.200701138.

35 R. J. C. Lima, P. T. C. Freire, J. M. Sasaki, A. P. Ayala, F. E. A. Melo and J. Mendes Filho, *et al.*, Temperature-dependent Raman scattering studies in $NaNbO_3$ ceramics, *J. Raman Spectrosc.*, 2002, **33**(8), 669–674, DOI: 10.1002/jrs.897.

36 Y. Shiratori, A. Magrez, J. Dornseiffer, F. H. Haegel, C. Pithan and R. Waser, Polymorphism in micro-, submicro-, and nanocrystalline $NaNbO_3$, *J. Phys. Chem. B*, 2005, **109**(43), 20122–20130, DOI: 10.1021/jp052974p.

37 D. Chapron, F. Cordero and M. D. Fontana, Characterization of oxygen vacancies in $SrTiO_3$ by means of anelastic and Raman spectroscopy, *J. Appl. Phys.*, 2019, **126**(15), 154101, DOI: 10.1063/1.5115106.

38 I. de Castro Silva, A. C. Reinaldo, F. A. Sigoli and I. O. Mazali, Raman spectroscopy-in situ characterization of reversibly intercalated oxygen vacancies in α-MoO_3, *RSC Adv.*, 2020, **10**(31), 18512–18518, DOI: 10.1039/d0ra01207f.

39 Y. K. Choi, T. Hoshina, H. Takeda, T. Teranishi and T. Tsurumi, Effects of oxygen vacancies and grain sizes on the dielectric response of $BaTiO_3$, *Appl. Phys. Lett.*, 2010, **97**(21), 212907, DOI: 10.1063/1.3508947.

40 T. Kobayashi and F. Narita, 158 Effects of grain size and oxygen vacancy density on the elastic and piezoelectric properties of $BaTiO_3$ polycrystals: phase field simulations. in *Proc. Comput. Mech. Conf.*, The Japan Society of Mechanical Engineers, 2015, vol. 28, p. 158-1, DOI: 10.1299/jsmecmd.2015.28._158-1_.

41 H. Xu, C. Liu, H. Li, Y. Xu, J. Xia and S. Yin, *et al.*, Synthesis, characterization and photocatalytic activity of $NaNbO_3$/ZnO heterojunction photocatalysts, *J. Alloys Compd.*, 2011, **509**(37), 9157–9163, DOI: 10.1016/j.jallcom.2011.06.100.

42 M. L. López, I. Álvarez-Serrano, A. Galdámez, E. Rodríguez-Aguado, E. Rodríguez-Castellón and Y. Saad, New dielectric anomalies in the A-site highly deficient $NaxNbO_3$ electroceramics, *Ceram. Int.*, 2020, **46**(10), 16770–16780, DOI: 10.1016/j.ceramint.2020.03.253.

43 B. Yang, J. Bian, L. Wang, J. Wang, Y. Du and Z. Wang, *et al.*, Enhanced photocatalytic activity of perovskite $NaNbO_3$ by oxygen vacancy engineering, *Phys. Chem. Chem. Phys.*, 2019, **21**(22), 11697–11704, DOI: 10.1039/C9CP01763A.

44 R. K. Sahu and S. Asthana, Enhancement of piezoelectric and ferroelectric response *via* tuning of relaxor and antiferroelectrics: insights from poling study, *J. Alloys Compd.*, 2025, **1010**, 178227, DOI: 10.1016/j.jallcom.2024.178227.

45 A. M. Ferraria, A. P. Carapeto and A. M. B. do Rego, X-ray photoelectron spectroscopy: silver salts revisited, *Vacuum*, 2012, **86**(12), 1988–1991, DOI: 10.1016/j.vacuum.2012.05.031.

46 S. Ardizzone, C. L. Bianchi, M. Fadoni and B. Vercelli, Magnesium salts and oxide: an XPS overview, *Appl. Surf. Sci.*, 1997, **119**(3–4), 253–259, DOI: 10.1016/S0169-4332(97)00180-3.

47 S. C. Johnson, Oxygen vacancies in $BaTiO_3$ have a surprising impact on dielectric and ferroelectric properties, *Scilight*, 2018, 150001, DOI: 10.1063/1.5033331.

48 K. Banerjee and S. Asthana, The effect of A-site cation on ferroelectric properties in $Na_{0.5}Bi_{0.5}TiO_3$-based materials: correlation between Burns temperature and remanent polarization, *J. Appl. Phys.*, 2020, **127**(14), 144102, DOI: 10.1063/1.5131201.

49 S. Chatterjee, A. Barman, S. Barman, T. Chabri, S. Kar-Narayan and A. Datta, *et al.*, Role of oxygen vacancies on the low-temperature dielectric relaxor behavior in epitaxial $Ba_{0.85}$Ca0.15Ti0.9Zr0.1O3 thin films, *Phys. Rev. Mater.*, 2021, **5**(6), 064415, DOI: 10.1103/PhysRevMaterials.5.064415.

50 S. Lanfredi, M. H. Lente and J. A. Eiras, Phase transition at low temperature in $NaNbO_3$ ceramic, *Appl. Phys. Lett.*, 2002, **80**(15), 2731–2733, DOI: 10.1063/1.1470260.

51 W. Cao and R. Gerhardt, Calculation of various relaxation times and conductivity for a single dielectric relaxation process, *Solid State Ionics*, 1990, **42**(3–4), 213–221, DOI: 10.1016/0167-2738(90)90010-O.

52 S. Havriliak and S. Negami, A complex plane representation of dielectric and mechanical relaxation processes in some polymers, *Polymer*, 1967, **8**, 161–210, DOI: 10.1016/0032-3861(67)90021-3.

53 S. Sahoo, P. K. Mahapatra and R. N. P. Choudhary, Colossal dielectric response, relaxation mechanism and multiferroic properties of $(Ba_{1-x}Sm_x)(Ti_{1-x}Fe_x)O_3$ $(0.0 \leq x \leq 0.5)$, *Mater. Sci. Eng. B*, 2020, **260**, 114624, DOI: 10.1016/j.mseb.2020.114624.

54 N. Pradhani, P. K. Mahapatra and R. N. P. Choudhary, Effect of cerium oxide addition on optical, electrical and dielectric characteristics of $(Bi_{0.5}Na_{0.5})TiO_3$ ceramics, *J. Phys. Mater.*, 2018, **1**(1), 015007, DOI: 10.1088/2515-7639/aacff0.

55 Q. Xu, H. Liu, Z. Song, X. Huang, A. Ullah and L. Zhang, *et al.*, A new energy-storage ceramic system based on $Bi_{0.5}Na_{0.5}TiO_3$ ternary solid solution, *J. Mater. Sci.: Mater. Electron.*, 2016, **27**, 322–329, DOI: 10.1007/s10854-015-3757-x.

56 J. Hao, Z. Xu, R. Chu, W. Li, D. Juan and F. Peng, Enhanced energy-storage properties of $(1-x)[(1-y)(Bi_{0.5}Na_{0.5})$-$TiO_{3-y}(Bi_{0.5}K_{0.5})TiO_3]$–$x$ $(K_{0.5}Na_{0.5})NbO_3$ lead-free ceramics, *Solid State Commun.*, 2015, **204**, 19–22, DOI: 10.1016/j.ssc.2014.12.004.

57 F. A. Kröger and H. J. Vink, Relations between the concentrations of imperfections in crystalline solids, in *Solid State Physics*, ed. F. Seitz and D. Turnbull, 1956, vol. 3, pp. 307–435, DOI: 10.1016/S0081-1947(08)60135-6.

58 E. A. V. Ferri, J. C. Sczancoski, L. S. Cavalcante, E. C. Paris, J. W. M. Espinosa and A. T. De Figueiredo, *et al.*, Photoluminescence behavior in $MgTiO_3$ powders with vacancy/distorted clusters and octahedral tilting, *Mater. Chem. Phys.*, 2009, **117**(1), 192–198, DOI: 10.1016/j.matchemphys.2009.05.042.

59 A. P. Kumar, D. Bilehal, A. Tadesse and D. Kumar, Photocatalytic degradation of organic dyes: Pd-γ-Al_2O_3 and PdO-γ-Al_2O_3 as potential photocatalysts, *RSC Adv.*, 2021, **11**(11), 6396–6406, DOI: 10.1039/d0ra10290c.

60 M. Khatun, P. Mitra and S. Mukherjee, Effect of band gap and particle size on photocatalytic degradation of $NiSnO_3$ nanopowder for some conventional organic dyes, *Hybrid Adv.*, 2023, **4**, 100079, DOI: 10.1016/j.hybadv.2023.100079.

61 M. Saha, P. P. Cho, C. Subrahmanyam, M. K. Niranjan and S. Asthana, Structural, dielectric, optical and photocatalytic properties of $(Na_{0.5}Bi_{0.5})ZrO_3$ lead-free perovskite: insights from experimental and *ab initio* theoretical studies, *J. Phys. D: Appl. Phys.*, 2024, **58**(8), 085304, DOI: 10.1088/1361-6463/ad98a5.

62 M. Saha, P. P. Cho, C. Subrahmanyam, M. K. Niranjan and S. Asthana, Comprehensive investigation of microstructure, electrical and photocatalytic properties of $K_{0.5}Na_{0.5}NbO_3$ lead-free ceramics prepared *via* different synthesis routes, *J. Mater. Sci.: Mater. Electron.*, 2023, **34**(33), 2214, DOI: 10.1007/s10854-023-11437-z.

63 M. Kumar, B. Meena, P. Subramanyam, G. Ummethala, S. R. K. Malladi and S. Dutta-Gupta, *et al.*, $CuInS_2$ nanosheet arrays with a MoS_2 heterojunction as a photocathode for PEC water splitting, *Energy Fuels*, 2023, **37**(3), 2340–2349, DOI: 10.1021/acs.energyfuels.2c03502.

64 P. P. Cho, P. P. Mon, M. Kumar, G. Madras and C. Subrahmanyam, Rational BiMoO nanospheres decorated g-C_3N_4 for photocatalytic performance of dye degradation, *Surf. Interfaces*, 2024, **50**, 104522, DOI: 10.1016/j.surfin.2024.104522.

65 F. Zhang, Y. Chen, W. Zhou, C. Ren, H. Gao and G. Tian, Hierarchical SnS_2/$CuInS_2$ nanosheet heterostructure films decorated with C_{60} for remarkable photoelectrochemical water splitting, *ACS Appl. Mater. Interfaces*, 2019, **11**(9), 9093–9101, DOI: 10.1021/acsami.8b21222.

66 P. A. Koyale, T. D. Dongale, S. S. Sutar, N. B. Mullani, A. G. Dhodamani and P. S. Takale, *et al.*, Boosting the photoelectrochemical performance of ZnO nanorods with Co-doped Zn-ZIFs metal-organic frameworks for water splitting studies, *Int. J. Hydrogen Energy*, 2024, **61**, 1294–1304, DOI: 10.1016/j.ijhydene.2024.02.216.

67 C. Liu, Y. Qiu, F. Wang, K. Wang, Q. Liang and Z. Chen, Design of core–shell-structured ZnO/ZnS hybridized with graphite-like C_3N_4 for highly efficient photoelectrochemical water splitting, *Adv. Mater. Interfaces*, 2017, **4**(21), 1700681, DOI: 10.1002/admi.201700681.